PHYSICAL REVIEW FLUIDS **3**, 104001 (2018)

Quasistatic fluid-fluid displacement in porous media: Invasion-percolation through a wetting transition

Bauyrzhan K. Primkulov,[1] Stephen Talman,[2] Keivan Khaleghi,[2] Alireza Rangriz Shokri,[2]
Rick Chalaturnyk,[2] Benzhong Zhao,[3] Christopher W. MacMinn,[4] and Ruben Juanes[1,*]
[1]*Department of Civil and Environmental Engineering, Massachusetts Institute of Technology,*
Cambridge, Massachusetts 02139, USA
[2]*Department of Civil and Environmental Engineering, University of Alberta,*
Edmonton, Alberta, Canada T6G 1H9
[3]*Department of Civil Engineering, McMaster University, Hamilton, Ontario, Canada L8S 4L7*
[4]*Department of Engineering Science, University of Oxford, Oxford OX1 3PJ, United Kingdom*

(Received 23 May 2018; published 11 October 2018)

We study the influence of wettability on the morphology of fluid-fluid displacement through analog porous media in the limit of vanishing flow rates. We introduce an invasion-percolation model that considers cooperative pore filling and corner-flow mechanisms and captures interface motion at the pore scale for all quasistatic flow regimes between strong drainage and strong imbibition. We validate the method against recent experimental observations of wetting transition in microfluidic cells patterned with circular posts and we use it to explore the sensitivity of fluid invasion to wettability heterogeneity, post spacing, and post height. Our model therefore extends the Cieplak-Robbins description of quasistatic fluid invasion by reproducing the wetting transition in strong imbibition, a feature that requires incorporating three-dimensional effects.

DOI: 10.1103/PhysRevFluids.3.104001

I. INTRODUCTION

Fluid-fluid displacement in porous media is a rich phenomenon, where the interplay between wettability, pore-scale disorder, viscosity ratio of invading and defending fluids, and magnitude of viscous forces relative to that of capillary forces (defined by the capillary number Ca) generates a wide spectrum of interface patterns. The study of the mechanisms behind these patterns is of relevance to many practical applications. For instance, in the limit of high capillary numbers, the displacement of high-viscosity fluid by a low-viscosity fluid develops a morphology akin to diffusion-limited aggregation [1–3] and hence serves as an analog system to dielectric breakdown [4], electrodeposition [5], and propagation of forest fires [6]. Furthermore, both high- and low-capillary-number displacement regimes have direct practical significance in soil remediation and chemical filters [7], fuel cell technology [8], carbon sequestration [9], oil recovery [10], and design of microfluidic devices [11].

For a given fluid pair, the wettability of the porous medium plays a fundamental role in defining the nature of the displacement at both pore [12–14] and macroscopic scales [15,16]. Wettability is often defined through the contact angle θ between the fluid-fluid interface and the solid. We adopt the convention that θ is measured from the invading phase such that $\theta > 90^\circ$ corresponds to drainage and $\theta < 90^\circ$ corresponds to imbibition. In the limit of low capillary number and strong drainage (i.e., strongly nonwetting invading fluid), the fluid-fluid interface advances through

---

[*] juanes@mit.edu

capillary fingering and forms a jagged interface that tends to trap defending fluid throughout the displacement [17–20]. In weak imbibition (i.e., weakly wetting invading fluid), in contrast, the interface tends to move as a compact front [15,16,21,22], where capillary forces work to flatten the interface through cooperative pore filling [23,24]. While the mechanisms of fluid-fluid displacement in drainage are fairly well explored, fluid-fluid displacement in imbibition continues to challenge our mathematical descriptions.

Patterned microfluidic devices offer a convenient way to visualize the fluid-fluid displacement in a controlled and repeatable environment. As a quasi-two-dimensional analog of natural porous media, these microfluidic devices are typically fabricated by generating a pattern of posts on a solid surface and confining it between two flat plates, allowing careful control of both pore geometry and wettability. Early microfluidic experiments [1,17–19] explored the interplay between viscous and capillary forces in drainage and weak imbibition, and their findings are in line with the theory [15,16,25,26]. Only recently has this body of work been extended to strong imbibition, where new displacement patterns emerge [27,28].

Zhao *et al.* [27] conducted a series of viscously unstable experiments on microfluidic devices with an irregular pattern of circular posts, where water displaced oil radially from the center of the flow cell at different injection rates and different contact angles between 150° (strong drainage) and 7° (strong imbibition). The authors reported a wetting transition in the strong imbibition regime ($7^\circ < \theta < 45^\circ$): Flow reverts from compact displacement to a corner-flow regime, where the invading fluid advances by preferentially coating the corners between the posts and top and bottom plates of the flow cell. Similar observations were recently reported on a regularly patterned microfluidic cell with square posts [28]. These findings may have significant implications for physical modeling of the displacement processes with tunable wetting conditions.

Several computational approaches are available to model pore-scale fluid-fluid displacement. These include, in decreasing order of fidelity (and required computational power) [29], (i) molecular dynamic simulations, (ii) numerical solutions of the Navier-Stokes equations with interface and contact-line tracking, (iii) lattice or dissipative particle dynamics based models, and (iv) pore-network models. The first three approaches require a detailed description of the pore geometry and are not yet practical for obtaining macroscopic invasion patterns. Pore-network models, on the other hand, rely on a simplified pore geometry and a simplified description of the flow and are therefore less computationally demanding [30]. The geometric details as well as simplifying assumptions of the interface vary widely from one study to another [31–34].

Two particular subclasses of pore-network models are of interest in reproducing the experimental observations of Zhao *et al.* [27] in the limit of very low Ca: invasion-percolation algorithms [19,20] and the quasistatic interface tracking method of Cieplak and Robbins [23,24]. Invasion-percolation algorithms are robust, but can only capture the invading interface morphology in strong drainage. The interface-tracking algorithm of Cieplak and Robbins [23,24] is applicable to wettabilities from strong drainage to weak imbibition, although it is susceptible to the biases of user-defined conventions in injection pressure increments and scanning order of pore-invasion mechanisms. Neither method extends to the corner-flow regime of strong imbibition.

Here we implement an invasion-percolation algorithm that qualitatively reproduces fluid-fluid displacement morphologies for all wettabilities, from strong drainage to strong imbibition. By building on the work of Cieplak and Robbins [23,24], we are able to explicitly calculate the critical pressures of pore-scale instabilities, including the instability events potentially responsible for the corner-flow regime in strong imbibition [27]. This approach eliminates the need for user-assigned pressure increments, instead advancing the interface in the manner of invasion-percolation. Our quasistatic algorithm captures the fluid-fluid displacement in the limit of very low Ca, where viscous forces can be neglected.

The algorithm was implemented on a two-dimensional flow geometry similar to the one in the experiments of Zhao *et al.* [27]. We used the model to capture the wetting transition in strong imbibition and explored the sensitivity of the flow pattern to pore-scale heterogeneity in contact angle, post spacing, and to three-dimensional effects of finite post height.

II. METHOD

Experimental observations of fluid-fluid displacement in different wettability regimes provide an intuitive way to understand the underlying assumptions behind different models of multiphase flow. In drainage, the invasion pattern advances by overcoming local capillary entry pressures within the porous medium [18]. In the limit of vanishing Ca, viscous dissipation can be neglected and the invasion process is well captured by the invasion-percolation algorithm [20,35,36]. This approach replaces the pore space with a network of nodes (pores) and edges (throats). Throats that contain a fluid-fluid interface are considered active. Every active throat is ranked according to its critical capillary pressure, which can be calculated from the throat size. The invading fluid moves by advancing locally into the throat with the lowest critical capillary pressure, resulting in invasion avalanches and displacement fronts that often loop on themselves and trap clusters of the defending fluid behind the advancing front.

While the invasion-percolation algorithm is in good agreement with experiments in drainage [18], it fails to reproduce the invading fluid pattern during imbibition. Here cooperative pore-filling mechanisms make the invading pattern smoother and invasion proceeds through compact fronts [19].

Cieplak and Robbins [23,24] showed that in order to capture cooperative pore-filling effects during imbibition one needs to account for the local pore geometry [23,24]. They approximated the porous medium by placing posts on a regular two-dimensional (2D) lattice; every post was assigned a random radius from a uniform distribution. The interface consisted of a collection of arcs between the posts. Every arc intersected nearby posts at a prescribed contact angle and curvature defined by the Laplace pressure Δp.

Cieplak and Robbins [23,24] introduced three types of instabilities: burst (no stable arc at given Δp), touch (interface touches opposite post), and overlap (two neighboring interfaces coalesce within the pore). The algorithm moves the fluid-fluid interface at fixed injection pressures by searching for unstable arcs and replacing them with new stable configurations (pore invasion). When no unstable arcs are found, the invading fluid pressure is increased to induce further advance.

Unlike the invasion-percolation algorithm, local interface instabilities are sensitive to geometric configurations of neighboring arcs, allowing for cooperative pore filling (mostly dominated by touch and overlap instabilities) during imbibition. Moreover, the algorithm produces results nearly identical to invasion-percolation algorithm in drainage, where burst instabilities are prevalent [24]. Thus, the model of Cieplak and Robbins [23,24] extends the description of quasistatic fluid-fluid displacement in porous media from strong drainage to weak imbibition.

At the same time, Cieplak and Robbins [23,24] acknowledged that the arbitrary sequence of pressure increments affects the morphology of simulated invasion fronts. Unlike the invasion-percolation algorithm, where the sequence of local interface advances is determined through global critical pressure ranking, the Cieplak-Robbins [23,24] model advances unstable arcs in the order they are discovered by a user-defined search convention. Moreover, the choice of pressure increments often results in more than one type of instability within the same arc; instabilities are removed by authors' convention where touch instabilities are removed first and burst instabilities are removed last.

We found that by reformulating the original approach of Cieplak and Robbins [23,24], one can explicitly calculate critical pressures of all instability events and advance the interface in an invasion-percolation-like manner. The interface moves based on the ranking of critical pressures that are calculated from local arc and post geometries. Thus, this formulation eliminates the need for arbitrary pressure increments and allows the least stable arcs to advance first. Below we describe the details of the formulation followed by the algorithm in the spirit of invasion-percolation.

Consider a set of neighboring posts (Fig. 1). On every image, posts are numbered from 1 to 3 (where applicable): The left post is 1, the right post is 2, and the top post is 3 [Figs. 1(b)–1(d)]. Each post is defined through its radius, location expressed in Cartesian coordinates, and a contact angle. For example, post 1 has radius r_1, location (x_1, y_1), and contact angle θ_1 measured from the invading fluid between posts 1 and 2 [Fig. 1(a)]. Without loss of generality, we rotate and translate

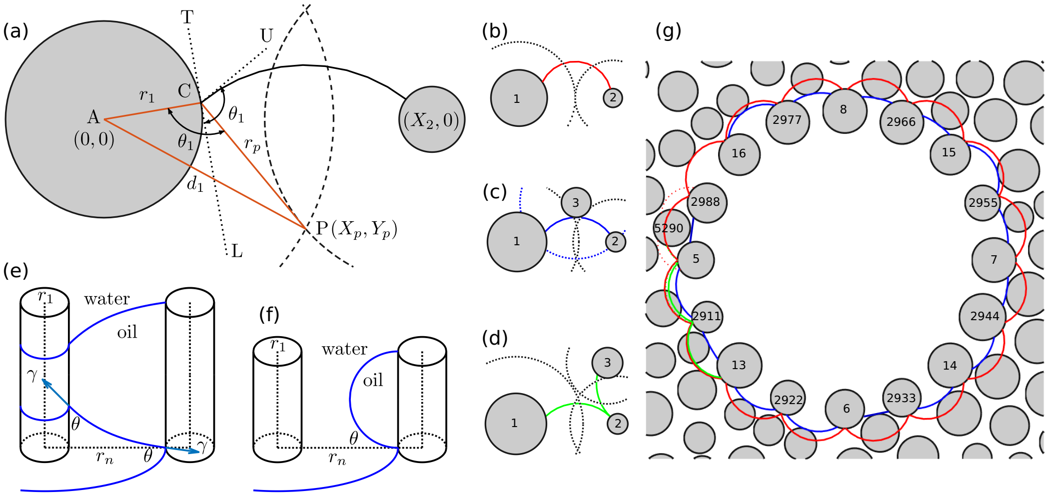

FIG. 1. (a) Invasion front configuration between two posts. (b) Burst event: An unstable interface (red line) advances into the pore. (c) Touch event: The interface touches the nearest post. (d) Overlap event: Two fronts (green lines) coalesce on the post surface and fill the pore. (e) Corner-flow event: The corner meniscus touches and coats the neighboring post. (f) Capillary bridge event: The corner menisci coalesce mid-post before reaching the next post. (g) Invading front configuration with post IDs: Red, blue, and green interfaces correspond to burst, touch, overlap critical interfaces, respectively.

the coordinate system so that points (x_1, y_1), (x_2, y_2), and (x_3, y_3) turn into (0,0), $(X_2, 0)$, and (X_3, Y_3).

For the description that follows, we assume that the posts are tall enough that the events considered in Figs. 1(b)–1(d) can be formulated in a two-dimensional sense. The validity and limitations of this assumption are further explored in Sec. III.

Consider an interface of radius of curvature r_p that meets post 1 at contact angle θ_1 [Fig. 1(a)]. We define d_1 to be the distance from the center of interface curvature to the center of post 1. Given an expression for value of $\angle ACP$, the distance d_1 can be determined from the law of cosines for $\triangle ACP$. Both $\angle PCU$ and $\angle TCA$ are equal to $\pi/2$ and $\angle UCT$ is $\pi - \theta_1$. Since $\angle ACP + \angle PCU + \angle UCT + \angle TCA = 2\pi$, then $\angle ACP = \theta_1$. Therefore,

$$d_1(r_p, \theta_1) = AP = \sqrt{r_1^2 + r_p^2 - 2r_1 r_p \cos\theta_1}. \tag{1}$$

Equation (1) defines the distance between the center of curvature (X_p, Y_p) and the center of post 1 (0,0). This means that the point (X_p, Y_p) lies on a circle concentric with post 1 and radius d_1, where the interface satisfies the contact angle θ_1 and has radius of curvature r_p. All points satisfying this requirement are shown as a dashed line in Fig. 1(a).

A similar construction for an interface intersecting with a second post of radius r_2 and a contact angle θ_2 centered at $(X_2, 0)$ defines a second circle centered at post 2. For a given r_p, this second circle [dashed line in Fig. 1(a) opening to the right] will share either two, one, or zero common points with the set of potential centers of curvature for the interfaces which stably contact post 1. Figure 1(a) shows a case where the interface is stable. Considering only the case when the invading fluid is sourced from below the X axis, the stable interface touching both posts will be centered at a point (X_p, Y_p) which is determined to simultaneously satisfy

$$X_p^2 + Y_p^2 = d_1(r_p, \theta_1)^2, \tag{2a}$$

$$(X_p - X_2)^2 + Y_p^2 = d_2(r_p, \theta_2)^2, \tag{2b}$$

$$Y_p \leqslant 0. \tag{2c}$$

Subtraction of (2a) and (2b) allows for the direct calculation of X_p and then Y_p can be trivially found as the negative root of Eq. (2a). Equation (2c) ensures that one selects the correct root when solving for Y_p [Fig. 1(a)].

The equations considered here are simplified significantly by the choice of post placement. For posts located at generic grid points, the post centers can be simply translated and subsequently rotated to achieve this configuration. Following calculations in this modified coordinate system, the results can be simply rotated and translated back to the original coordinate system.

We are now ready to define several instability events that determine interface propagation. Following the work of Cieplak and Robbins [23,24], we consider burst, touch, and overlap events and we additionally introduce a different class of corner events. The order and frequency of these pore-level events ultimately define the shape of the quasistatic invasion pattern. Below we find the critical Laplace pressures Δp (corresponding to radius of curvature r_p via the Young-Laplace equation $1/r_p = \Delta p/\gamma$) at which each event takes place.

A. Burst event

As the pressure of the invading phase increases, the radius of interface curvature r_p decreases. This results in lower values for both d_1 and d_2. As a result, increasing Δp reduces the radii of the dashed lines in Fig. 1(a) and the number of their intersection points [solutions for Eq. (2)] changes from 2 to 1 and eventually 0. This means that there is no longer a stable interface between posts 1 and 2; this event is referred to as burst [see Fig. 1(b)]. The burst event coincides with the last stable configuration of the interface between two posts at given contact angles θ_1 and θ_2. This occurs when there is only a single root to Eq. (2) and also corresponds to the case when $Y_p = 0$ (which implies a zero discriminant in the quadratic equation). Introducing this condition in Eq. (2) allows finding the critical radius of curvature r_p that corresponds to burst as a tangential intersection of dashed circles in Fig. 1(a):

$$X_p^2 = d_1(r_p, \theta_1)^2, \tag{3a}$$

$$(X_p - X_2)^2 = d_2(r_p, \theta_2)^2. \tag{3b}$$

Equations (3) can be rearranged to give a quadratic equation in r_p, with the burst radius chosen to yield a positive burst pressure.

B. Touch event

The touch event refers to the configuration depicted in Fig. 1(c). Here the interface tangentially intersects the third post centered at (X_3, Y_3) and with radius r_3. This configuration can be viewed as the intersection of black dotted lines and the circle of radius $r_p + r_3$ centered at (X_3, Y_3), represented by the blue dotted line in Fig. 1(c):

$$X_p^2 + Y_p^2 = d_1(r_p, \theta_1)^2, \tag{4a}$$

$$(X_p - X_2)^2 + Y_p^2 = d_2(r_p, \theta_2)^2, \tag{4b}$$

$$(X_p - X_3)^2 + (Y_p - Y_3)^2 = (r_p + r_3)^2. \tag{4c}$$

Equations (4) can be solved analytically for the critical value of r_p that satisfies the touch condition. Again, the touch condition given by the solution of Eqs. (4) can be reduced to a quadratic equation in r_p, although the expansion to this form involves some laborious algebra.

C. Overlap event

Cieplak and Robbins [23,24] defined the overlap event as an instability where two advancing contact lines meet on the surface of a post [see Fig. 1(d)]. The solution to the overlap radius of

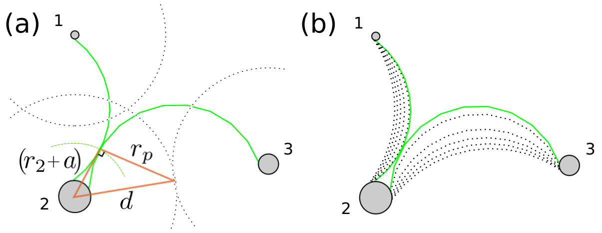

FIG. 2. (a) Schematic diagram of meniscus coalescence away from the post surface. (b) Drainage overlap at $\theta > 90^\circ$: Menisci coalesce inside the pore space, leaving trapped oil on the wall of the invaded post.

curvature can be written as the intersection of three circles, the interface between posts 1 and 2, the interface between posts 2 and 3, and the circle corresponding to the surface of post 2,

$$(X - X_{p12})^2 + (Y - Y_{p12})^2 = r_p^2, \tag{5a}$$

$$(X - X_{p23})^2 + (Y - Y_{p23})^2 = r_p^2, \tag{5b}$$

$$(X - X_2)^2 + Y^2 = r_2^2. \tag{5c}$$

Here (X_{p12}, Y_{p12}) and (X_{p23}, Y_{p23}), which are also functions of r_p, denote the centers of curvature for interfaces between posts 1 and 2 and posts 2 and 3, respectively. Equations (5) coupled with solutions for (X_{p12}, Y_{p12}) and (X_{p23}, Y_{p23}) can be solved numerically for a critical value of r_p.

The underlying assumption in the above equations is that both interfaces in Fig. 1(d) have the same radius of curvature r_p. In a quasistatic process, as assumed here, the pressure is spatially uniform in both invading and defending fluids with a Laplace pressure drop between them. Thus, we can assume that $\Delta p_{12} = \Delta p_{23}$ in overlap event calculations. Therefore, from the Young-Laplace equation, we have that $\frac{\gamma}{r_{p12}} = \frac{\gamma}{r_{p23}}$ or $r_{p12} = r_{p23} = r_p$.

D. Drainage overlap event

The original definition of overlap event by Cieplak and Robbins [24] is valid only for $\theta \leqslant 90^\circ$. When $\theta > 90^\circ$, the two menisci coalesce away from the post, trapping some defending liquid on the post wall [11], as illustrated for $\theta = 120^\circ$ in Fig. 2(b). This effect has been largely ignored in pore-level simulations and a careful experimental investigation was only reported recently by Lee *et al.* [11].

Consider the drainage overlap configuration in Fig. 2(a), where overlap occurs at $\theta > 90^\circ$ and a distance a away from post 2. The solution for this coalescence can be obtained as an intersection of the two menisci and a circle of radius $(r_2 + a)$ concentric with post 2:

$$(X - X_{p12})^2 + (Y - Y_{p12})^2 = r_p^2, \tag{6a}$$

$$(X - X_{p23})^2 + (Y - Y_{p23})^2 = r_p^2, \tag{6b}$$

$$(X - X_2)^2 + Y^2 = (r_2 + a)^2. \tag{6c}$$

Noting that $(r_2 + a)^2 = d^2 - r_p^2$, where d^2 is analogous to Eq. (1), unknown a can be eliminated from the above expressions. This allows solving drainage overlap numerically for the critical value of r_p.

E. Corner and capillary bridge events

In addition to the events described above, all of which, apart from overlap for $\theta > 90^\circ$, had already been identified previously [23,24], Zhao *et al.* [27] experimentally observed a transition from pore invasion in weak imbibition to corner flow in strong imbibition. In order to capture this transition it is necessary to consider the shape of the fluid-fluid interface in three dimensions. When the solid walls have high affinity for the invading liquid, the liquid accumulates in corners between the posts and the top and bottom plates of the cell, adopting a constant-curvature configuration shown in Fig. 1(e).

In our model, a corner event occurs when the interface swells sufficiently to touch a neighboring post; this allows flow towards the corner of the neighbor post. The distance from the center of the wetted post to the surface of its nearest neighbor is denoted by r_n. This distance can be estimated from a force balance on the corner liquid in the vertical direction [37]

$$2r_1 \cos\theta_1 - 2r_n \sin\theta_1 + \left(r_n^2 - r_1^2\right)\Delta p/\gamma = 0. \tag{7}$$

Equation (7) can be used to determine the critical pressure differential across the interface that is required for a corner event for every post on the invasion front. This equation is valid when the height of the posts is significantly taller than the spacing between the posts.

When the post height is comparable to the post spacing, the top and bottom corner menisci might intersect in the middle of the post before a corner event. This results in the coalescence of the two interfaces, and invading liquid coats the post in the shape of a capillary bridge [Fig. 1(f)]. In this case, we use the constant interface curvature equation shown in Appendix A to find the pressure at which mid-post coalescence takes place. A more detailed discussion of the corner liquid interface shape and validity of Eq. (7) is given in Appendix A.

F. Invasion algorithm

The closest analog to the invasion algorithm presented here is the invasion-percolation method [20,35,36], where the invasion front advances by overcoming threshold pressures associated with pore throats. At every step, a pore with the lowest threshold pressure gets invaded first; the interface is updated and the algorithm proceeds to the next invasion step. The simplicity of invasion-percolation leaves very little room for misinterpretation, but it has traditionally been applied only in strong drainage.

The quasistatic invasion of the fluid-fluid interface is governed entirely by the critical pressures of burst, touch, overlap, and corner events. To illustrate how the pore-level threshold pressures combine to determine the evolution of the invasion front, consider the initial configuration in Fig. 1(g). This initial invasion front is obtained by connecting the innermost posts, a procedure which does not necessarily produce a stable front. Here every post has an identification number.

We calculate the critical invasion pressures for pore-scale events by solving Eqs. (3)–(7) for every post on the invasion front. To advance the invading fluid, we traverse the invasion front and select the post with the smallest critical invasion pressure Δp [e.g., a touch instability for the interface at post 5 in Fig. 1(g)].

The manner in which the invasion front changes following an event depends on the type of instability that takes place. If a burst or touch instability occurs, the nearest post to the interface is added to the invasion front [Figs. 1(b) and 1(c)]. If the least stable event is overlap, the post where the contact lines meet is removed from the invasion front.

Finally, if a corner flow event occurs, a newly captured post is added to the list of corner invasion posts. We keep track of this list separately from all other events because the manner in which corner menisci advance is distinctly different. As we show later, this leads to competition between corner invasion and cooperative pore-filling invasion at some contact angles, leading to the transition in pore-level displacement mechanism observed by Zhao *et al.* [27]. We assume that cooperative pore-filling front posts are also coated in their corners, so the corner list is at least as long as the other list, an assumption that is reasonable for the quasistatic description we employ here, but which will likely be inaccurate at very high capillary numbers, when viscous forces dominate and films of the defending fluid are left behind.

By following these simple rules, one can capture the complexity of invasion patterns and their relation to substrate wettability. Although this method was built with the framework initially proposed by Cieplak and Robbins [24] in mind, there are several features of our approach that are important to note.

First, the evolution of the interface in the algorithm of Cieplak and Robbins [24] was somewhat sensitive to the arbitrary selection of pressure increments and the order in which the invasion mechanisms were scanned. In the Cieplak-Robbins [24] study, after each pressure increment, every interface was scanned for burst, touch, and overlap in sequence and an unstable interface was allowed a single step forward. This means that the natural order of the instability events could be disturbed with a poor choice of pressure increments or scanning order, a shortcoming acknowledged by the authors [23,24]. In contrast, our algorithm always advances the *least stable* interface within the invasion front, therefore eliminating arbitrariness.

Second, by maintaining the list of critical pressures, new computations only need to be performed in the neighborhood of newly invaded pores. This feature may prove to be especially useful should the algorithm be extended to a dynamic invasion front (i.e., when taking into consideration the pressure changes associated with viscous forces during the motion of the invasion front as in Ref. [31]).

Finally, within the current framework, we can easily assign unique contact angles to individual posts. We utilize this feature to generate different realizations of the same invasion experiment. That is, for every realization, we assign a random contact angle for every post from a narrow distribution centered around a global mean. This brings us closer to experimental conditions, where small local deviations from the average contact angle of the substrate exist due to material impurities and inhomogeneity from the fabrication process.

III. RESULTS AND DISCUSSION

We use the model described in the preceding section to address the following objectives. (i) We test whether our method is able to fully capture the invasion-pattern morphology through the wetting transition from strong drainage to strong imbibition. (ii) We explore the sensitivity of the wetting transition to local perturbations in contact angles through pore-level event statistics and the macroscopic fractal dimension. (iii) We study the links between pore spacing and mechanisms of pore-level displacement. (iv) Finally, we explore the limits of our model by introducing three-dimensional effects with finite post heights within the flow geometry.

The baseline pore geometry used in this work was generated in a similar manner to Zhao *et al.* [27]. MATLAB's `pdemesh` was used to generate a circular Hele-Shaw cell configuration with a diameter of 15 cm. Centers of the posts were placed at the nodes of the generated irregular mesh. Then the radius of each individual post was assigned to 45% of the smallest edge at a corresponding node. The final geometry of posts and the histograms of the resulting post radii and throat sizes are shown in Fig. 3.

A. Invasion front morphology through the wetting transition

We simulated radial invasion of water into the oil-filled microfluidic cell described above, with substrate contact angles between 160° (strong drainage) and 10° (strong imbibition). Pore-invasion simulations in Fig. 4 demonstrate that the morphology of the invasion pattern depends strongly on the wettability of the substrate. In particular, the invasion pattern becomes more compact as the scenario changes from strong drainage ($\theta = 160^\circ$) to weak imbibition ($\theta = 45^\circ$) and this is accompanied by a reduction in the amount of trapped oil behind the invasion front. In strong imbibition, the invading fluid starts to preferentially accumulate in the corners formed by the posts with the top and bottom plates. This results in an invasion mechanism that competes with burst, touch, and overlap events.

Consider a single post with invading liquid accumulating in its corners with top and bottom plates. As the pressure of the invading fluid increases, the size of the corner meniscus increases,

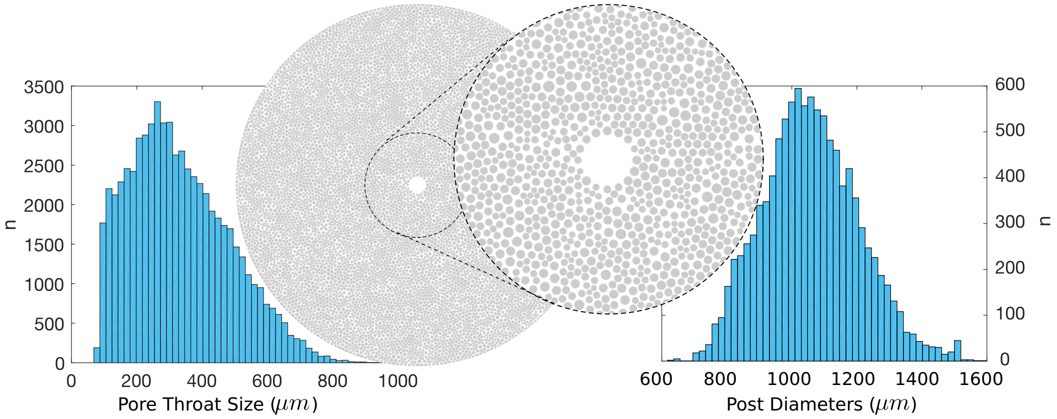

FIG. 3. Generated pore geometry along with post diameter and pore throat size histograms. Posts were placed on irregular triangular lattice generated with MATLAB's `pdemesh` and post radii were assigned to 45% of the smallest connected edge.

and at some critical pressure the liquid extends far enough to reach the post's closest neighbor. At this point, the invading liquid flows into the corner of the next post. Here invasion proceeds akin to invasion-percolation, albeit on a dual network, where the sites are the posts and the links are the edges of the corresponding Delaunay tessellation. This mode of invasion leads to fingering patterns, in contrast with the compact invasion characteristic of weak imbibition. The pattern at $\theta = 40^\circ$ in Fig. 4 is particularly noteworthy: Here frequencies of cooperative pore-filling and corner-flow events are comparable and the invasion front advances in a mixed regime.

More generally, the invading front morphology in Fig. 4 can be classified into three categories: (i) invasion-percolation in strong drainage (mostly burst events, $\theta = 160^\circ$), (ii) cooperative pore filling in weak imbibition (mostly touch and overlap events, $\theta = 45^\circ$), and (iii) post chaining due to corner-flow or capillary bridge events in strong imbibition ($\theta = 10^\circ$). The first two categories take place at contact angles between 160° and 45° and they are very much in line with the quasistatic simulations of Cieplak and Robbins [23,24]. The latter category was experimentally observed only recently [27].

Furthermore, we find that the finger width measurements (Fig. 12) of the emerging patterns are in line with experimental observations [15,16,27] and numerical predictions [23,24]. In strong drainage, the invading patterns have finger width comparable to the size of a typical pore. When the flow is dominated by cooperative pore-filling events, the finger width diverges to a size of about 18 pores. Finally, the finger width reduces to a fraction of a pore size in the corner-flow-dominated

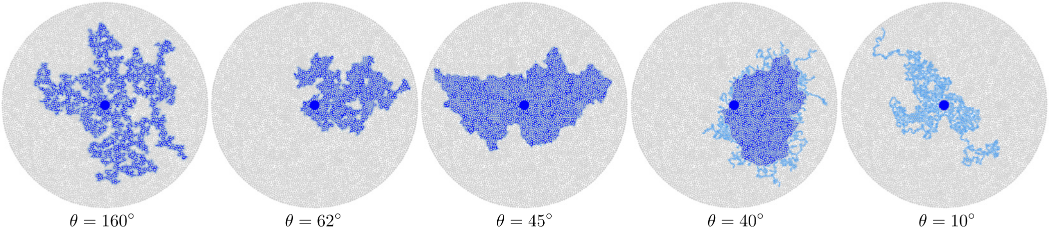

FIG. 4. Immiscible fluid invasion simulation results: The algorithm presented in Sec. II covers the full range of pore wettabilities, from strong drainage ($\theta = 160^\circ$) to strong imbibition ($\theta = 10^\circ$). Dark blue regions represent fully invaded pores; light blue regions represent partially invaded pores with coated post corners. We include video files of the invasion process at different wettabilities in the Supplemental Material [38].

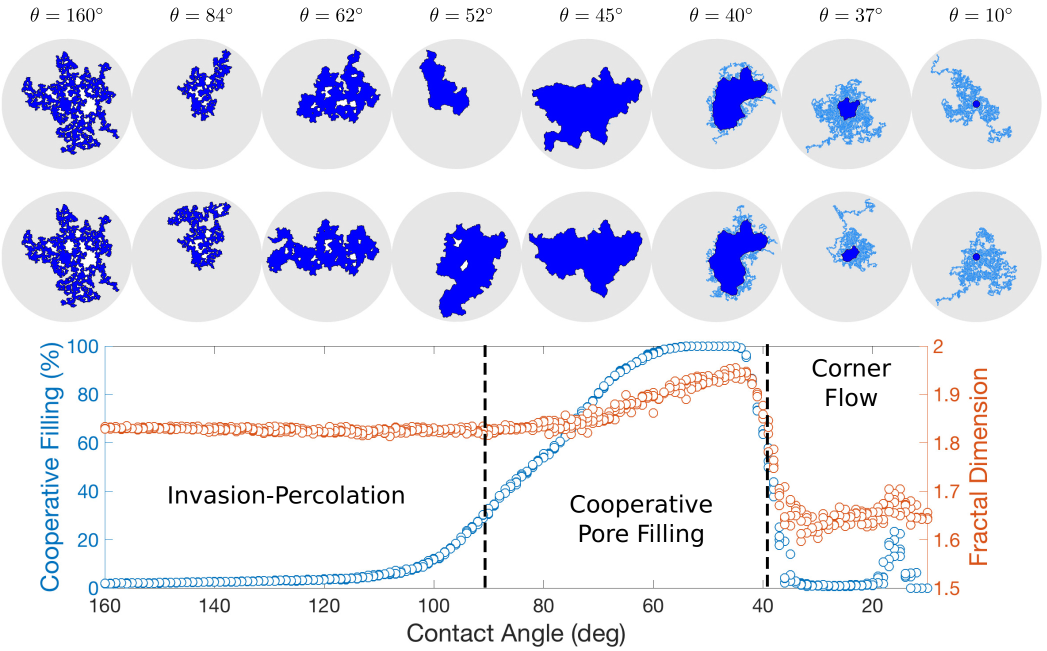

FIG. 5. Cooperative pore-filling and fractal dimension plots, showing invasion patterns for different realizations at each fixed global contact angle. As the system moves from strong drainage ($\theta = 160^\circ$) to weak imbibition ($\theta = 45^\circ$), the percentage of cooperative pore-filling events gradually increases. The transition from weak to strong imbibition is marked with a sharp drop in both fraction of cooperative pore-filling events and fractal dimension.

regime. We include the detailed discussion on finger width measurements in Appendix C and we include video files of the invasion process at different wettabilities in the Supplemental Material [38].

B. Sensitivity of macroscopic invasion to local contact angle perturbations

Any real substrate is bound to have imperfections that perturb local contact angles from the global mean. In the context of the experiments by Zhao *et al.* [27], local imperfections in contact angle could arise from dust deposition on the substrate during fabrication of the microfluidic cell and one typically takes a great deal of care in minimizing these effects.

In practice, no two invasion tests look exactly the same, even when conducted following the same experimental protocol. However, while different realizations of the same experimental conditions can be expected to produce nonidentical invasion patterns, those patterns should possess a common quality. This raises an interesting question of quantifying the similarity of the invasion patterns.

We mimic local imperfections in contact angle by assigning unique contact angles to every post in the flow geometry. In particular, we select the contact angles from a uniform distribution with 2° range centered around the global mean. Figure 5 presents the summary from multiple realizations. Every experiment was repeated four times for contact angles between 160° and 10°, producing four different realizations for each set of invasion conditions.

The degree of similarity of the resulting invasion patterns was assessed by means of two metrics: (i) the percentage of cooperative pore-filling events (touch and overlap) and (ii) the fractal dimension of the invasion pattern. The fractal dimension was calculated using the box-counting method [39,40]. The details of the box-counting calculations are included in Appendix B.

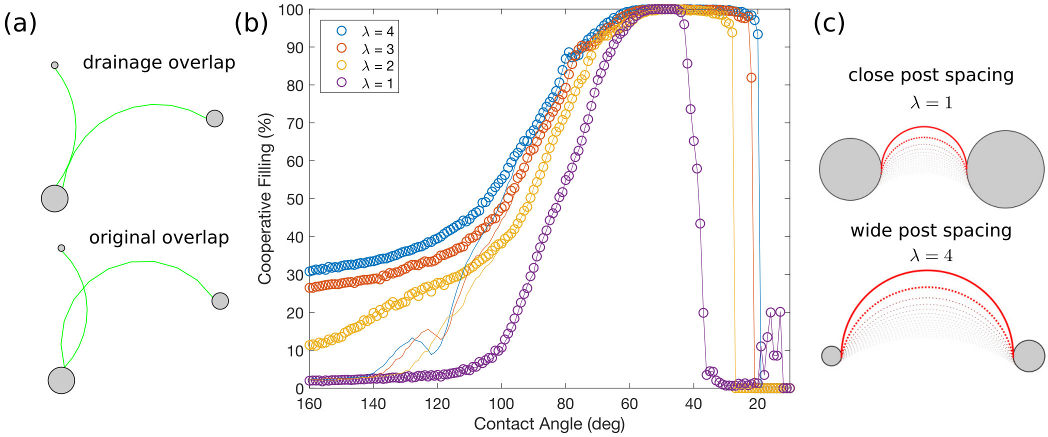

FIG. 6. (a) Schematic diagrams of the drainage overlap and overlap event of Cieplak and Robbins [23,24]. (b) Percentage of cooperative pore-filling events for posts spaced out by a factor of λ from the original post geometry. The colored circles represent simulations with drainage overlap considered; solid lines represent simulations with the original overlap definition of Cieplak and Robbins [23,24]. (c) Schematic diagram of post spacing and the fluid-fluid interface.

The results in Fig. 5 demonstrate that the percentage of cooperative pore-filling events is a robust classifying metric for the invasion shapes; it exhibits negligible variability among realizations. As the contact angle changes from 160° to 45°, touch and overlap events become dominant. At contact angles below 45°, corner-flow events take over.

In contrast, the fractal dimension shows a higher variability from one realization to another, and here we can appreciate the difference in invasion shapes quantitatively. For example, consider the two realizations with $\theta = 84^\circ$ in Fig. 5. At a glance, the two invasion patterns look similar, but there are subtle differences in the invaded regions and clusters of trapped oil. The fractal dimension reflects this difference, resulting in appreciable scatter of points at $\theta = 84^\circ$ in Fig. 5.

The fractal dimension data reported in Fig. 5 are computed with box-counting method and show reasonable values for all flow regimes. The mean fractal dimension for invasion-percolation is 1.83, for cooperative pore filling it is between 1.83 and 1.96, and in the corner-flow regime it is 1.65.

Overall, we were able to mimic the simulation of the same experimental conditions with local imperfections in the wetting properties of the substrate. While every simulation produces a unique pattern, each pattern falls into one of the shape categories (invasion-percolation, cooperative filling, and corner flow) based on the percentage of cooperative pore-filling events plot.

C. Influence of drainage overlap and post spacing on cooperative pore filling

Consider the schematic diagrams of drainage overlap and the original overlap events in Fig. 6(a). During the invasion process, the drainage overlap always precedes the original overlap event of Cieplak and Robbins [23,24] and thus corresponds to a lower critical pressure. Since we advance the invasion front into pores with lowest critical pressures, by overestimating the critical pressures of overlap events, one would erroneously advance the invasion front through spurious burst instabilities. This is especially likely to happen when the spacing between the posts is large. We examine the significance of drainage overlap by increasing the spacing between posts in the original pore geometry by a factor $\lambda > 1$.

Figure 6(b) shows that by considering drainage overlap, we recover a considerable number of cooperative pore-filling events otherwise lost if one follows the original definition of overlap event of Cieplak and Robbins [23,24]. Simulations with drainage overlap result in about 30% cooperative pore-filling event ratio at $\theta = 160^\circ$ for $\lambda = 4$, while the original overlap produces no cooperative filling events at $\theta = 160^\circ$ for all λ.

One can intuitively understand why larger spacing between posts increases the frequency of cooperative pore-filling events by examining two posts and a fluid-fluid interface between them at $\lambda = 1$ and $\lambda = 4$ [Fig. 6(c)]. In drainage, as the pressure of the invading fluid increases, the interface approaches its burst configuration. When the spacing between the posts is small ($\lambda = 1$), the fluid-fluid interface remains mainly within the gap between the two posts. In contrast, when the spacing is wide ($\lambda = 4$), the interface extrudes significantly away from the gap between two posts before reaching the burst configuration. As a result, this interface is more likely to encounter (and coalesce with) the neighboring fluid interfaces. In the extreme limit, when $\lambda \gg 1$, we expect the fluid front to advance mainly through cooperative pore filling via drainage overlap events, even in strong drainage. Therefore, the drainage overlap presented in Sec. II is crucial for the validity of the quasistatic invasion model on a wide range of pore geometries, especially in simulating multiphase flow through highly porous materials such as low-density micropillar arrays [21] or fibrous media [41–43].

The drainage overlap events (see Sec. II) result in trapping of the defending liquid on the surfaces of the posts at $\theta > 90^\circ$ [Fig. 2(b)]. Furthermore, the earlier onset of cooperative pore filling due to λ changes the amount and the manner in which the defending fluid is trapped behind the invasion front. Trapping of the defending liquid is an interesting problem on its own, but it is not the focus of this work.

D. Three-dimensional effects: Out-of-plane curvature

In the simulations described so far, we neglected the out-of-plane curvature contributions in the Young-Laplace equation when calculating critical pressures of burst, touch, and overlap events in Sec. II, akin to the simulations of Cieplak and Robbins [23,24]. The ascribed correction to the critical pressures is that $\frac{\Delta p}{\gamma} = \frac{1}{r_p}$ is replaced by $\frac{\Delta p}{\gamma} = \frac{1}{r_p} - \frac{2\cos\theta}{h}$ for burst, touch, and overlap events.

As the height of the posts decreases, the relative magnitudes of the critical pressures change. This in turn alters the final patterns of the invasion fronts (Fig. 7). As the post heights approach 100 μm, the critical pressures of burst, touch, and overlap events become lower than critical pressures of corner and capillary bridge flow events, leading to a dominance of cooperative pore filling at low contact angles. However, in reality, Zhao *et al.* [27] observed the corner-flow-dominated regime at $\theta = 7^\circ$.

This discrepancy between the experiment and our quasistatic simulations can be due to several factors. First, this out-of-plane curvature adjustment is rather crude and was only implemented to test the limits of our 2D model. A full three-dimensional consideration of the invasion would be more accurate, although the formulation would also be significantly more complex. Second, and perhaps more importantly, we have likely overestimated the critical pressures of corner events. This can be appreciated from a close examination of invasion progression at strong imbibition in the experiments of Zhao *et al.* [27]. There, on average, corner menisci appeared to grow only up to about the middle of pore throats, at which point the neighboring posts were coated. In our model, the critical pressures of corner-flow events were calculated assuming the full growth of the corner meniscus across the throat, which results in higher critical pressures. Indeed, imposing the half-throat rule in our model produces a transition to corner flow at around $\theta = 22^\circ$. This earlier coating of the posts could be due to the establishment of a conductive film ahead of the corner meniscus that was not visible in the experimental images. Indeed, the fluid invasion through thin-film flow in strong imbibition and accumulation of invading fluid in the corners was also observed by Odier *et al.* [28]. Resolving the detailed dynamics of post bridging in the strong imbibition regime warrants further experimental and theoretical investigations.

Furthermore, solid surface roughness in realistic 3D rock geometries may provide continuity to the wetting layers. In the presence of strong surface roughness, growth of the corner menisci would still dominate in strong imbibition, but the morphology of the invading pattern would likely

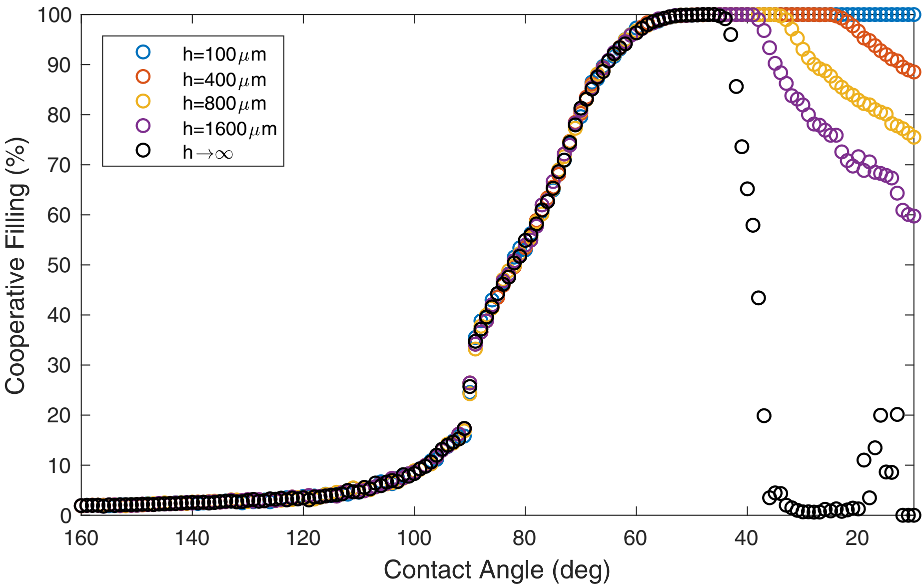

FIG. 7. Figure showing how post heights alter the shapes of the invasion fronts: The onset of the corner-flow-dominated regime is heavily influenced by the out-of-plane curvature correction of the burst, touch, and overlap instabilities. The magnitude of the correction is controlled by the height of the posts. Invasion fronts on the right are plotted for different h at $\theta = 10^\circ$.

be controlled by the heterogeneity in surface roughness rather than the spacing between the posts. While the considerations of roughness and film flow in realistic 3D geometries are outside the scope of this work, they are, however, potentially important mechanisms in strong imbibition.

IV. CONCLUSION

Overall, our approach to immiscible fluid invasion in disordered micropillar arrays can be viewed as an extension of the invasion-percolation algorithm to include wettability through critical invasion pressures for cooperative filling and corner-flow events. This approach eliminates the need for (and thus the sensitivity to) arbitrary increments in the invading pressures and scanning order of the interface for instability events observed in the earlier work [23,24]. Our algorithm also allows assigning a unique contact angle to every post, to study the sensitivity of the invasion patterns to local wettability variations.

The invasion model presented here was coded into an efficient simulation algorithm, making it an attractive starting point for dynamic pore-invasion simulations. A natural way of extending this algorithm is through incorporating viscous forces with a coupled pore-network model [31,44,45].

We have tested the invasion model by comparing the simulation outputs with the experiments of Zhao *et al.* [27]. Our quasistatic model was able to capture the nature of the invasion fronts at low capillary numbers for the full range of substrate wettabilities, including the transition from invasion-percolation to *cooperative filling* to *corner flow* as a function of contact angle. This can have important implications in enhanced oil recovery, carbon sequestration, and microfluidic applications. For example, in petroleum production, a more compact invasion pattern is preferred when displacing oil from the reservoir by water injection. In some instances of reactive transport in microfluidic applications, however, one might want to induce the fingering invasion to maximize the interface area between invading and defending liquids.

Fluid injection can result in localized redistribution of stress loads within porous media accompanied by dilation of the pore space [44,45]. Some of the recent experimental observations

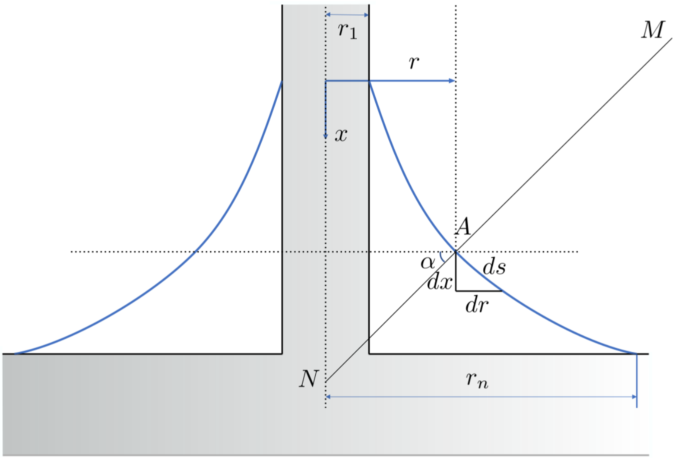

FIG. 8. Shape of the corner meniscus around the post with radius r_1. Here AM and AN are the principal radii of curvature at point A, where AM is in plane and AN is perpendicular to the plane.

of pore-scale poroelasticity include localized fluid-induced deformation of hydrogel packs [46] and glass bead pack deformation caused by immiscible liquid infiltration [47–49]. The dynamic extension of the model presented here could be further extended to include pore deformations due to changes in effective stress under different wettability conditions, which could capture the potential interplay between pore wettability and deformation during fluid-fluid displacement.

ACKNOWLEDGMENTS

We would like to thank Amir Pahlavan for insightful discussions. This work was partly funded by the US Department of Energy (Grant No. DE-SC0018357).

APPENDIX A: CORNER MENISCUS

In this Appendix we examine the shape of the corner meniscus around a typical post. We follow a similar derivation to that of the droplet shape on a fiber [37]. We treat our post as a fiber and impose desired contact angles as boundary conditions at the interface ends, imposing that contact angles of θ are maintained at both post and plate contacts. Finally, we examine the growth and potential mid-post coalescence of the top and bottom menisci.

1. Corner meniscus shape

Here we determine how far the meniscus extends in the horizontal and vertical directions for a given Laplace pressure and check whether the force balance equation suggested in this work adequately captures the horizontal extent of the meniscus. Figure 8 shows a cross section of the corner meniscus around a post with radius r_1. By developing an argument very similar to the formulation of the droplet shape on a fiber of de Gennes *et al.* [37], we can find the meniscus shape equation. We start with the Young-Laplace equation for an arbitrary point A on the liquid interface

$$\frac{1}{AN} - \frac{1}{AM} = \frac{\Delta p}{\gamma}. \tag{A1}$$

Noting that $r = AN\cos\alpha$ and $ds = AM d\alpha$, Eq. (A1) can be written as

$$\frac{\cos\alpha}{r} - \frac{d\alpha}{ds} = \frac{\cos\alpha}{r} - \frac{d\alpha}{dr}\frac{dr}{ds} = \frac{\Delta p}{\gamma}. \tag{A2}$$

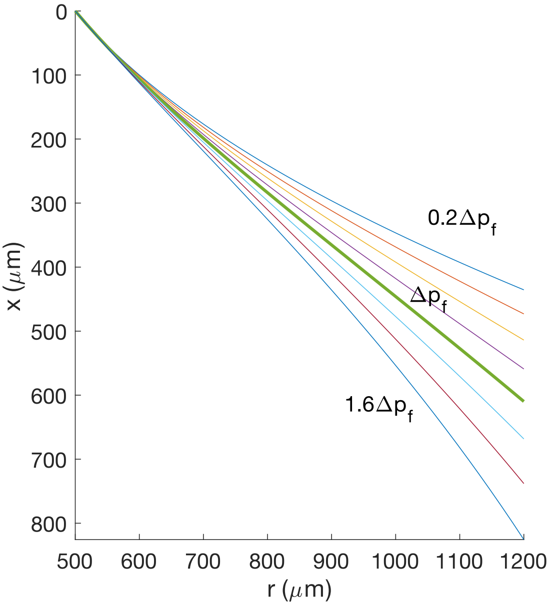

FIG. 9. Interface shape of a corner meniscus outside a post. Equation (A7) is solved with $\theta = 40^\circ$, $r_1 = 500\ \mu$m, and $r_n = 1200\ \mu$m. Here Δp_f represents the Laplace pressure obtained from the force balance equation (7). The condition $\dot{x}(r_n) = \tan\theta_1$ is exactly satisfied when $\Delta p = \Delta p_f$.

Furthermore, $dr = \sin\alpha ds$, so the Young-Laplace equation takes the form

$$\frac{\cos\alpha}{r} - \frac{d\alpha}{dr}\sin\alpha = \frac{\Delta p}{\gamma}. \tag{A3}$$

Noting that $dr = \sin\alpha ds$ and $dx = \cos\alpha ds$,

$$\frac{dx}{dr} = \dot{x} = \cot\alpha. \tag{A4}$$

Squaring both sides of Eq. (A4) leads to the equations

$$\sin\alpha = \frac{1}{(1+\dot{x}^2)^{1/2}}, \tag{A5a}$$

$$\cos\alpha = \frac{\dot{x}}{(1+\dot{x}^2)^{1/2}}. \tag{A5b}$$

Differentiating Eq. (A4) with respect to r yields

$$\ddot{x} = -\frac{1}{\sin^2\alpha}\frac{d\alpha}{dr}. \tag{A6}$$

Finally, substituting Eqs. (A5) and (A6) into Eq. (A3), we obtain the final equation for the liquid interface

$$\frac{\dot{x}}{r(1+\dot{x}^2)^{1/2}} + \frac{\ddot{x}}{(1+\dot{x}^2)^{3/2}} = \frac{\Delta p}{\gamma}. \tag{A7}$$

Now Eq. (A7) with $\dot{x}(r_1) = \cot\theta_1$ and $x(r_1) = 0$ can be used to find the corner meniscus profile. Figure 9 shows the solution of Eq. (A7) for $r = (r_1, r_n)$ with a typical geometry and contact angle used in this study.

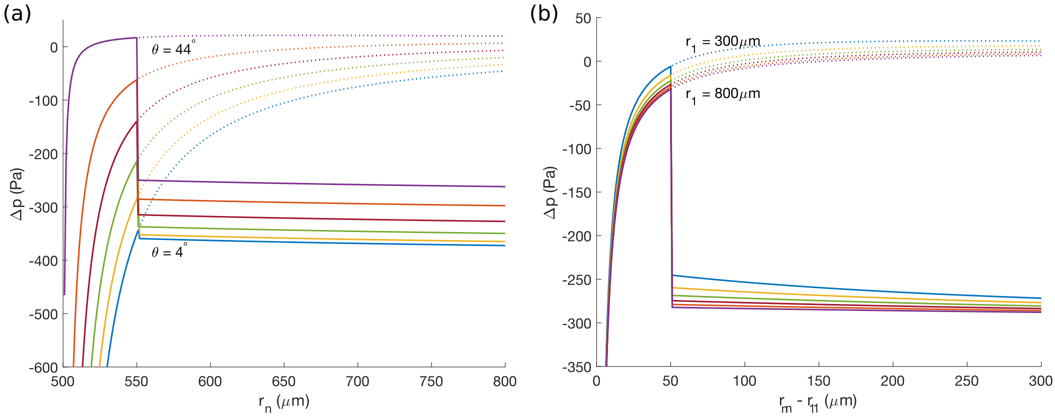

FIG. 10. Laplace pressure for a growing corner meniscus. Initially, the invading liquid is confined to the corners. As the horizontal extent of the liquid grows, the top and bottom corners meet at the mid-height of the post and the shape changes into a capillary bridge. This transition point corresponds to the negative jump in Laplace pressure. (a) Evolution of the corner menisci for contact angles between 4° and 44° and $r_1 = 500\ \mu$m. (b) Evolution of the corner menisci for post radii between 300 and 800 μm and a contact angle of 40°.

The pressure drop across the interface should be such that $\dot{x}(r_n) = \tan\theta_1$. It turns out that this condition is exactly satisfied when Δp is calculated from the force balance equation (7). This verifies the validity of the force balance approach in finding critical values of Δp for corner flow.

At the same time, Fig. 9 shows that the extent of the corner meniscus is of comparable size in horizontal and vertical directions. Since the height of the posts in the Zhao *et al.* [27] experiments is 100 μm, we need to consider two cases: (i) corner menisci at the top and bottom that do not touch and (ii) corner menisci that meet and merge at the mid-height of the cell. When the liquid menisci do not meet in the middle of the post, the critical Δp for corner flow can be estimated from the force balance equation (7). However, when corner liquids meet, the shape of the interface can be estimated as a capillary bridge between two flat plates, described by the equation [37]

$$\frac{1}{r_n - \frac{h}{2\cos\theta_1}(1 - \sin\theta_1)} - \frac{2\cos\theta_1}{h} = \frac{\Delta p}{\gamma}. \tag{A8}$$

2. Corner meniscus growth

We now consider the growth of the corner meniscus on a post with a height of 100 μm [Fig. 10(a)]. At first, the invading liquid is confined to the top and bottom corners of the post; growth of the meniscus in the horizontal direction increases the Laplace pressure requirement. Top and bottom menisci grow to the point that they touch at mid-height of the post. At this point, the shape of the corner liquid changes into a capillary bridge.

We make the following observations. First, before the menisci merge, the Laplace pressure increases with growing r_n. After they merge, the shape turns into a capillary bridge and the Laplace pressure decreases with growing r_n. This means that if the liquid invasion was stimulated with small pressure increments, the corner liquid would grow gradually with increasing Δp and then grow spontaneously after assuming a capillary bridge shape.

Second, the magnitude of the discontinuity in Δp at the corner liquid merger point is smaller at low contact angles [Fig. 10(a)]. This can be explained intuitively by visualizing the corner merging instant at contact angles of 0° and 45°. For $\theta = 0°$, when two corner liquids meet at the mid-height of the post, $\frac{dr}{dx}|_{x=h/2} = 0$ both before and after the merger. However, for $\theta = 45°$, $\frac{dr}{dx}|_{x=h/2} = 1$

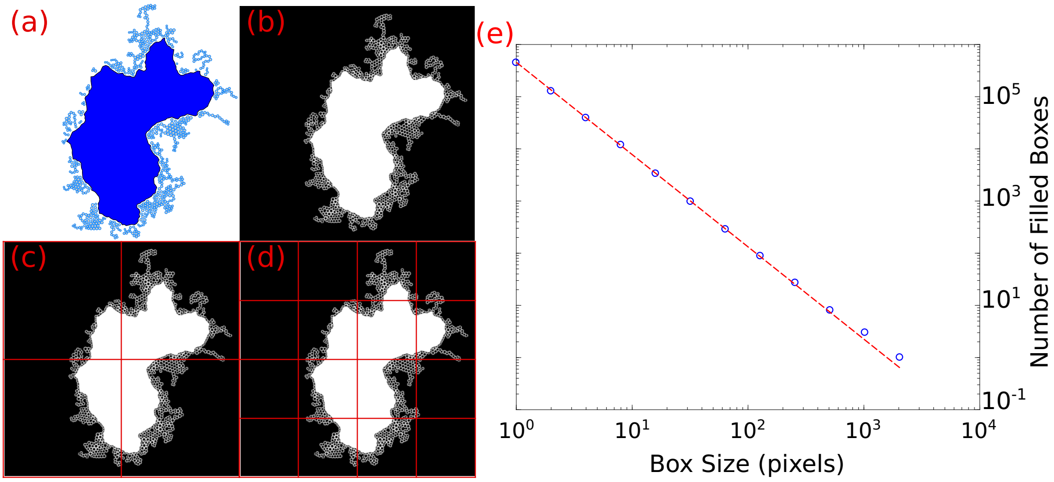

FIG. 11. Fractal dimensions calculated with the box-counting method: (a) color image (1200 × 1200 pixels) produced by the invasion algorithm for $\theta = 40^\circ$, (b)–(d) black and white versions of the invasion pattern placed on a grid of size $\epsilon = [1, n_{\text{pix}}]$, and (e) fractal dimension measured as a slope of number N of filled boxes against ϵ on a log-log plot, with the slope calculated from points with $\epsilon = [1, \frac{n_{\text{pix}}}{8}]$.

before and $\frac{dr}{dx}|_{x=h/2} = 0$ after the merger. This means that at 45° the invading liquid needs to snap from the corner to bridge shape. The magnitude of this snap is small at contact angles near 0°.

Finally, Fig. 10(b) shows that the Laplace pressure is smaller for larger posts. The out-of-plane radius of curvature (AN in Fig. 8) is always greater than the radius of the post and hence posts with greater radius correspond to lower Laplace pressures [Eq. (A1)]. In other words, it is easier to grow the corner menisci around the posts with larger radius.

APPENDIX B: MEASURING FRACTAL DIMENSION

The morphology of the invading fluid phase can be complex (Fig. 4) and fractal dimension can be an intuitive way to capture this complexity. Fractal dimension can be thought of as an index of the scale dependence of a pattern [39]. In this work, we utilize the box-counting method [39,40] to estimate the fractal dimension of the invading fluid patterns.

The box-counting method iteratively tiles the image containing the flow pattern with boxes of size ϵ. Each iteration uses increasingly greater value of ϵ and measures the number N of boxes that contain (or directly cover) the flow pattern. The magnitude of the slope of N against ϵ on a log-log plot defines the box-counting fractal dimension [40].

To estimate the fractal dimension of the invading fluid we took the following steps. (i) We obtained the invasion pattern image from the simulation, with fully surrounded posts treated as part of the invading phase [Fig. 11(a)]; this step typically produced images of 1200 × 1200 pixels in size. (ii) We converted the image to black and white [Fig. 11(b)]. (iii) We grid the image with boxes of size ϵ between 1 and the number of pixels in each direction of the image (n_{pix}) [Figs. 11(c) and 11(d)]. (iv) We recorded the number N of boxes required to fill the pattern for each ϵ. (v) We calculated the fractal dimension as an absolute value of the slope of N against ϵ on a log-log plot [Fig. 11(e)].

When calculating the slope of N against ϵ on the log-log plot, we imposed user-defined expectations on the bounds of the fractal behavior. We exclude the boxes close to the image size, so we set $\epsilon < \frac{n_{\text{pix}}}{8}$.

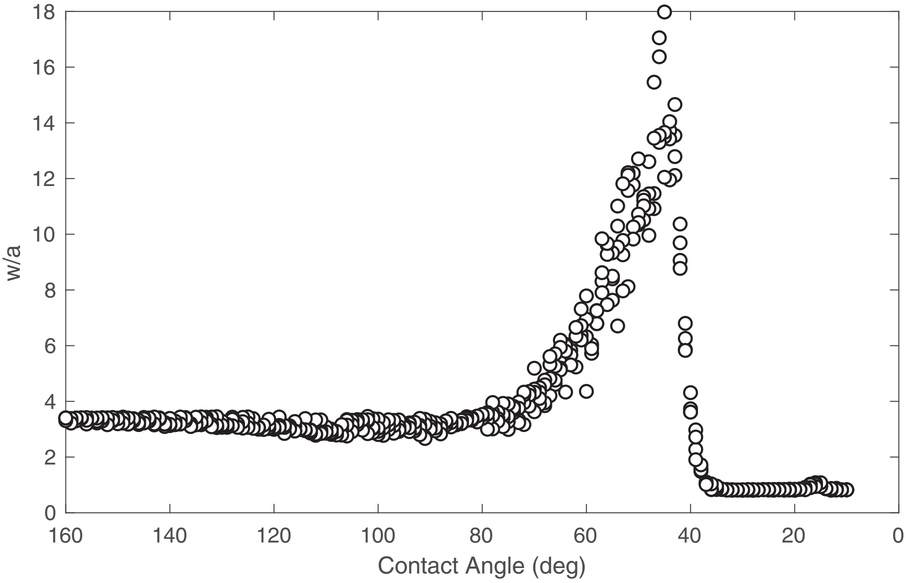

FIG. 12. Ratio of the invading pattern finger width to mean pore size, estimated in analogy to the work of Cieplak and Robbins [23,24].

APPENDIX C: MEASURING FINGER WIDTH

In order to estimate the invading fluid finger width w, Cieplak and Robbins [23,24] put forward the following method. First, they sliced the invasion pattern along the nodes of their regular lattice. Then they measured the size of the invaded region clusters along each 1D slice. The mean size of the clusters was taken as an estimate of w, which was then divided by the lattice length a.

We cannot follow the method of Cieplak and Robbins [23,24] precisely since our post geometry was built on an irregular lattice. We use a close equivalent estimate of w instead. We start with black and white images used to measure box-counting fractal dimension and slice it into separate rows. We collect the statistic of the invading clusters in resulting slices using MATLAB's `bwconncomp` function, where the mean size of the clusters estimates w in pixels. We repeat the same procedure on an image where pore spaces and posts have white and black colors, respectively. This allows estimating a as an average pore size in pixels. Thus, we recover the w/a used by Cieplak and Robbins. The above procedure was repeated for vertical slices as well.

Figure 12 shows that the finger width spans several pores in the invasion-percolation regime and starts diverging at contact angles below 60°. This growth of finger width is abruptly interrupted below 40°, where fluid invasion is dominated by corner flow and w is only a fraction of the mean pore size a.

[1] J.-D. Chen and D. Wilkinson, Pore-Scale Viscous Fingering in Porous Media, Phys. Rev. Lett. **55**, 1892 (1985).

[2] K. J. Måløy, J. Feder, and T. Jøssang, Viscous Fingering Fractals in Porous Media, Phys. Rev. Lett. **55**, 2688 (1985).

[3] L. Paterson, Diffusion-Limited Aggregation and Two-Fluid Displacements in Porous Media, Phys. Rev. Lett. **52**, 1621 (1984).

[4] L. Niemeyer, L. Pietronero, and H. J. Wiesmann, Fractal Dimension of Dielectric Breakdown, Phys. Rev. Lett. **52**, 1033 (1984).

[5] P. Meakin, S. Tolman, and A. Blumen, Diffusion-limited aggregation, Proc. R. Soc. London Ser. A **423**, 133 (1989).

[6] M. Conti and U. M. B. Marconi, Diffusion limited propagation of burning fronts, WIT Trans. Ecol. Envir. **137**, 37 (2010).

[7] S. Hill, Channeling in packed columns, Chem. Eng. Sci. **1**, 247 (1952).

[8] R. Anderson, L. Zhang, Y. Ding, M. Blanco, X. Bi, and D. P. Wilkinson, A critical review of two-phase flow in gas flow channels of proton exchange membrane fuel cells, J. Power Sources **195**, 4531 (2010).

[9] Y. Cinar, A. Riaz, and H. A. Tchelepi, Experimental study of CO_2 injection into saline formations, SPE J. **14**, 588 (2009).

[10] L. W. Lake, *Enhanced Oil Recovery* (Prentice-Hall, Englewood Cliffs, 1989).

[11] H. Lee, A. Gupta, T. A. Hatton, and P. S. Doyle, Creating Isolated Liquid Compartments Using Photopatterned Obstacles in Microfluidics, Phys. Rev. Appl. **7**, 044013 (2017).

[12] R. L. Hoffman, A study of the advancing interface, J. Colloid Interface Sci. **50**, 228 (1975).

[13] B. Levaché and D. Bartolo, Revisiting the Saffman-Taylor Experiment: Imbibition Patterns and Liquid-Entrainment Transitions, Phys. Rev. Lett. **113**, 044501 (2014).

[14] B. Zhao, A. Alizadeh Pahlavan, L. Cueto-Felgueroso, and R. Juanes, Forced Wetting Transition and Bubble Pinch-Off in a Capillary Tube, Phys. Rev. Lett. **120**, 084501 (2018).

[15] J. P. Stokes, D. A. Weitz, J. P. Gollub, A. Dougherty, M. O. Robbins, P. M. Chaikin, and H. M. Lindsay, Interfacial Stability of Immiscible Displacement in a Porous Medium, Phys. Rev. Lett. **57**, 1718 (1986).

[16] M. Trojer, M. L. Szulczewski, and R. Juanes, Stabilizing Fluid-Fluid Displacements in Porous Media through Wettability Alteration, Phys. Rev. Appl. **3**, 054008 (2015).

[17] R. Lenormand, C. Zarcone, and A. Sarr, Mechanisms of the displacement of one fluid by another in a network of capillary ducts, J. Fluid Mech. **135**, 337 (1983).

[18] R. Lenormand and C. Zarcone, Invasion Percolation in an Etched Network: Measurement of a Fractal Dimension, Phys. Rev. Lett. **54**, 2226 (1985).

[19] R. Lenormand, E. Touboul, and C. Zarcone, Numerical models and experiments on immiscible displacements in porous media, J. Fluid Mech. **189**, 165 (1988).

[20] R. Chandler, J. Koplik, K. Lerman, and J. F. Willemsen, Capillary displacement and percolation in porous media, J. Fluid Mech. **119**, 249 (1982).

[21] M. Jung, M. Brinkmann, R. Seemann, T. Hiller, M. S. de La Lama, and S. Herminghaus, Wettability controls slow immiscible displacement through local interfacial instabilities, Phys. Rev. Fluids **1**, 074202 (2016).

[22] K. Singh, H. Scholl, M. Brinkmann, M. Di Michiel, M. Scheel, S. Herminghaus, and R. Seemann, The role of local instabilities in fluid invasion into permeable media, Sci. Rep. **7**, 444 (2017).

[23] M. Cieplak and M. O. Robbins, Dynamical Transition in Quasistatic Fluid Invasion in Porous Media, Phys. Rev. Lett. **60**, 2042 (1988).

[24] M. Cieplak and M. O. Robbins, Influence of contact angle on quasistatic fluid invasion of porous media, Phys. Rev. B **41**, 11508 (1990).

[25] P. G. Saffman and G. Taylor, The penetration of a fluid into a porous medium or Hele-Shaw cell containing a more viscous liquid, Proc. R. Soc. London Ser. A **245**, 312 (1958).

[26] R. L. Chuoke, P. van Meurs, and C. van der Poel, The instability of slow, immiscible, viscous liquid-liquid displacements in permeable media, Petrol. Trans. AIME **216**, 188 (1959).

[27] B. Zhao, C. W. MacMinn, and R. Juanes, Wettability control on multiphase flow in patterned microfluidics, Proc. Natl. Acad. Sci. USA **113**, 10251 (2016).

[28] C. Odier, B. Levaché, E. Santanach-Carreras, and D. Bartolo, Forced Imbibition in Porous Media: A Fourfold Scenario, Phys. Rev. Lett. **119**, 208005 (2017).

[29] P. Meakin and A. M. Tartakovsky, Modeling and simulation of pore-scale multiphase fluid flow and reactive transport in fractured and porous media, Rev. Geophys. **47**, RG3002 (2009).

[30] M. J. Blunt, Flow in porous media—Pore-network models and multiphase flow, Curr. Opin. Colloid Interface Sci. **6**, 197 (2001).

[31] R. Holtzman and E. Segre, Wettability Stabilizes Fluid Invasion Into Porous Media Via Nonlocal, Cooperative Pore Filling, Phys. Rev. Lett. **115**, 164501 (2015).

[32] R. Holtzman, Effects of pore-scale disorder on fluid displacement in partially-wettable porous media, Sci. Rep. **6**, 36221 (2016).

[33] M. J. Blunt, Physically-based network modeling of multiphase flow in intermediate-wet porous media, J. Petrol. Sci. Eng. **20**, 117 (1998).

[34] M. S. Al-Gharbi and M. J. Blunt, Dynamic network modeling of two-phase drainage in porous media, Phys. Rev. E **71**, 016308 (2005).

[35] R. Lenormand and S. Bories, Description d'un mecanisme de connexion de liaision destine a l'etude du drainage avec piegeage en milieu poreux, C. R. Acad. Sci. **291B**, 279 (1980).

[36] D. Wilkinson and J. F. Willemsen, Invasion percolation: A new form of percolation theory, J. Phys. A: Math. Gen. **16**, 3365 (1983).

[37] P.-G. de Gennes, F. Brochard-Wyart, and D. Quéré, *Capillarity and Wetting Phenomena: Drops, Bubbles, Pearls, Waves* (Springer Science + Business Media, New York, 2013).

[38] See Supplemental Material at http://link.aps.org/supplemental/10.1103/PhysRevFluids.3.104001 for videos of the invasion process at different wettabilities.

[39] N. C. Kenkel and D. J. Walker, Fractals in the biological sciences, Coenoses **11**, 77 (1996).

[40] P. M. Iannaccone and M. Khokha, *Fractal Geometry in Biological Systems: An Analytical Approach* (CRC, Boca Raton, 1996).

[41] R. L. Peek, Jr. and D. A. McLean, Capillary penetration of fibrous materials, Ind. Eng. Chem. **6**, 85 (1934).

[42] K. E. Thompson, Pore-scale modeling of fluid transport in disordered fibrous materials, AIChE J. **48**, 1369 (2002).

[43] R. B. Calhoun and A. Mortensen, Infiltration of fibrous preforms by a pure metal, Metall. Trans. A **23**, 2291 (1992).

[44] A. K. Jain and R. Juanes, Preferential mode of gas invasion in sediments: Grain-scale mechanistic model of coupled multiphase fluid flow and sediment mechanics, J. Geophys. Res.: Solid Earth **114**, B08101 (2009).

[45] R. Holtzman and R. Juanes, Crossover from fingering to fracturing in deformable disordered media, Phys. Rev. E **82**, 046305 (2010).

[46] C. W. MacMinn, E. R. Dufresne, and J. S. Wettlaufer, Fluid-Driven Deformation of a Soft Granular Material, Phys. Rev. X **5**, 011020 (2015).

[47] M. J. Dalbe and R. Juanes, Morphodynamics of Fluid-Fluid Displacement in 3D Deformable Granular Media, Phys. Rev. Appl. **9**, 024028 (2018).

[48] R. Holtzman, M. L. Szulczewski, and R. Juanes, Capillary Fracturing in Granular Media, Phys. Rev. Lett. **108**, 264504 (2012).

[49] M. Trojer, P. de Anna, and R. Juanes (unpublished).